

Interaction of alpha particles in the lead region near the Coulomb barrier*

A. R. Barnett[†] and J. S. Lilley

J. H. Williams Laboratory of Nuclear Physics, University of Minnesota, Minneapolis, Minnesota 55455

(Received 7 January 1974)

The (α, n) cross section on ^{208}Pb and ^{209}Bi has been measured between 16 and 24 MeV by observing the α activity of the residual nuclei ^{211}Po and ^{212}At . The relative yields to both the ground and metastable states of each residual nucleus were obtained and new half-life determinations have been made for these states. The absolute yield was measured at 20 and 22 MeV to normalize the relative data. Below the $(\alpha, 2n)$ threshold, $\sigma(\alpha, n)$ constitutes most of the total reaction cross section, and the (α, n) data, together with accurate elastic scattering measurements at 19, 20, and 22 MeV are reproduced well by a six-parameter optical model. The fits are sensitive to the reaction cross-section data, and serve to define the magnitude and shape of the real potential at a radial distance of about 11 fm. The real potential in this region dominates the interaction at the present energies. The imaginary potential is relatively small; it is not well determined and serves only to absorb those waves which penetrate the real potential. The real potential obtained is interpreted in terms of an α -folding model using a free α -nucleon two-body force. The potential near the peak of the Coulomb barrier is determined primarily by the target matter density near 9 fm, where it is approximately 1% of its value at the center of the nucleus. Implications concerning the relative distributions of target neutron and protons are discussed.

<p style="margin: 0;">NUCLEAR REACTIONS ^{208}Pb, $^{209}\text{Bi}(\alpha, \alpha)$ (α, n); measured $\sigma(\theta)$ elastic, E_α $= 19, 20, 22$ MeV; $\sigma_{\alpha n}(E)$, $E_\alpha = 16-24$ MeV; $T_{1/2}$: ^{211}Po, $^{211}\text{Po}^m$, ^{212}At, $^{212}\text{At}^m$. Deduced optical potentials, surface matter density form factors.</p>
--

I. INTRODUCTION

The α particle was used in the earliest determinations of nuclear size and it may prove still to be one of the most useful probes for learning about the shape of the nucleus. It is a complex particle and, in principle, interacts in a more complicated way than nucleons do. However, its attenuation in nuclear matter restricts the interaction to the low-density surface region of the nucleus particularly if the α -particle bombarding energy is not too great. Thus, in the surface, the fact that the α particle has high binding energy, zero spin, and zero isospin may lead to a relatively uncomplicated interpretation of its interactions with the nuclear matter, and to some information on nucleon densities.

In the present studies, the bombarding energy is close to the Coulomb barrier height, and under these conditions, electrical repulsion constrains the interaction to the barrier region. The results, therefore, should be particularly sensitive to surface details and to barrier penetrabilities, which so strongly dominate evaporation and α -decay processes.

Elastic scattering is the easiest quantity to measure but it is dominated at low energies by Rutherford scattering. The angular distributions are rather featureless and extremely accurate

measurements are needed to detect specifically nuclear effects. The situation is quite different if nuclear reactions can be detected and, in particular, the total reaction cross section (σ_R) is related directly to the over-all nuclear interaction. Indeed, below the barrier it is considerably more important than elastic scattering in its sensitivity to the form of the interaction.¹

In general, it is extremely difficult to make an accurate determination of σ_R for α particles, especially at low energies. In very special cases, such as for α particles incident on ^{208}Pb and ^{209}Bi , the measurements are relatively straightforward since each important channel leads to an α -active product, which can be unambiguously identified and measured. Below the $(\alpha, 2n)$ thresholds, which occur at 19.9 MeV for ^{208}Pb and at 20.7 MeV for ^{209}Bi , the only important reaction channel is (α, n) . Inelastic scattering is known to be small^{2,3} (approximately 0.3 mb at 19 MeV) and is dominated by Coulomb excitation, which can be calculated. Other possible reaction channels are (α, p) and (α, γ) , and these also lead to characteristic α -active nuclei. The first is expected to be negligible because of the proton Coulomb barrier, and no evidence has been seen for either reaction. Thus, below the $(\alpha, 2n)$ threshold, the value of $\sigma(\alpha, n)$ should be a good measure of the total reaction cross section. This quantity has been determined

for both ^{208}Pb and ^{209}Bi between 16- and 24-MeV bombarding energy (Sec. II).

If the incident energy exceeds a certain value, deviations from pure Rutherford scattering become significant. In the α - ^{208}Pb system, this occurs² near 18 MeV, which is well below the peak of the nuclear-plus-Coulomb potential of 20.6 MeV, and corresponds to an interaction radius of $1.78 \times (A_1^{1/3} + A_2^{1/3})$ fm. An extensive and accurate series of elastic scattering measurements has been carried out for both ^{208}Pb and ^{209}Bi above 19 MeV (Sec. II). These data, together with the (α, n) results, were analyzed to obtain information about the α -particle interaction in the periphery of these nuclei. Section III discusses the analysis while in Sec. IV various conclusions are drawn.

II. EXPERIMENTAL

A. Elastic scattering

The elastic scattering measurements include data for both ^{208}Pb and ^{209}Bi taken at bombarding energies of 19, 20, and 22 MeV. Following the global analysis of these results as described in Sec. III, the scattering by ^{209}Bi at 22 MeV was repeated with higher precision and including more forward angles. Details of the experimental procedures are given below.

1. Scattering by lead and bismuth at 19, 20, and 22 MeV

Between 300 and 500 nA of α particles accelerated by the University of Minnesota MP Tandem Van de Graaff were used to bombard carbon-backed targets of ^{209}Bi and ^{208}Pb , each approximately $100 \mu\text{g}/\text{cm}^2$ thick.

The scattered particles were recorded using an array of four 700- μm Ortec surface-barrier detectors, set at 10° intervals on a precision ring which were fitted into a 43-cm Ortec scattering chamber. The angular intervals between the detectors and the relative angular position of the ring were determined to 0.1° . The geometrical solid angle of each detector, defined by an accurately machined aperture, was approximately 0.64 msr. Each detector was coupled to its own analog-to-digital converter (ADC) and signals from all ADC's were stored and analyzed using the on-line system of the CDC 3100 computer.

The beam was collected in a deep magnetically shielded Faraday cup, and measured with a current integrator which was calibrated to an accuracy of 0.1%. In addition, the scattered beam intensity was monitored by a fixed detector at 60° which provided a continuous check of possible target deterioration or beam movements.

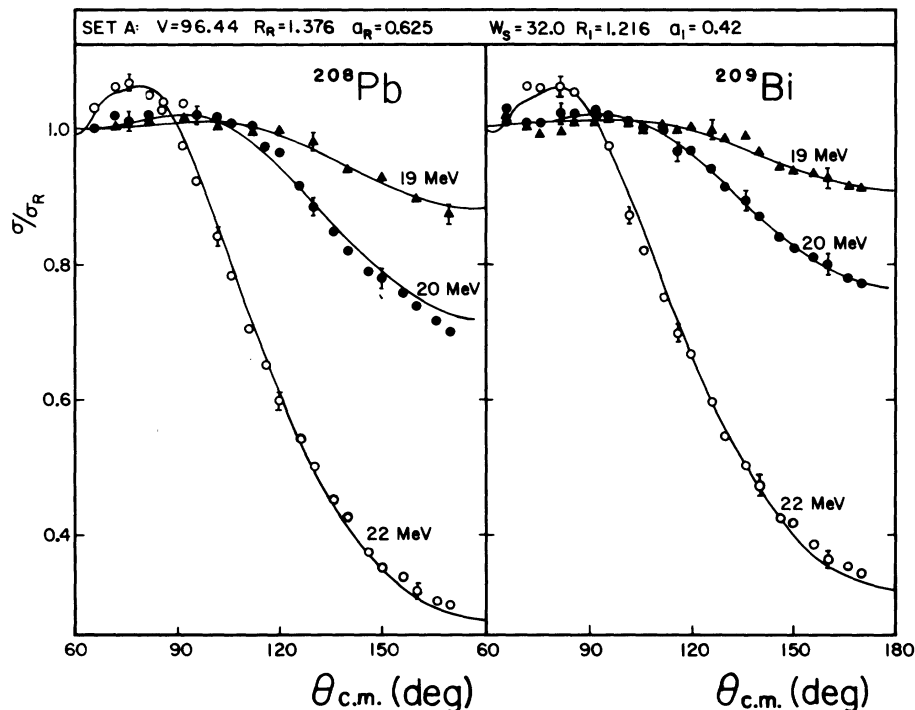


FIG. 1. Elastic differential cross sections, relative to Rutherford, of α particles scattered by ^{208}Pb and ^{209}Bi at 19, 20, and 22 MeV. The solid curves are optical-model calculations using the parameters: Set A listed at the top of the figure.

Data were taken at 5° intervals between 65 and $170^\circ(\text{lab})$, with frequent overlap runs to check the relative detector efficiencies. The elastic peak count required little or no background subtraction and relative errors of 2% or better were obtained. Dead-time corrections (less than 2% in general) were estimated from the known characteristics of the ADC's.

The absolute normalization was established at 16 MeV. A complete angular distribution taken at this energy followed the Rutherford law, within the experimental errors, over the entire angular range, thereby checking the over-all consistency of the technique. The 19-, 20-, and 22-MeV data are shown in Fig. 1. The absolute uncertainty for each distribution is 2%.

2. Precision elastic scattering by ^{209}Bi at 22 MeV

The later and more accurate measurements with α particles at 22 MeV on ^{209}Bi were taken

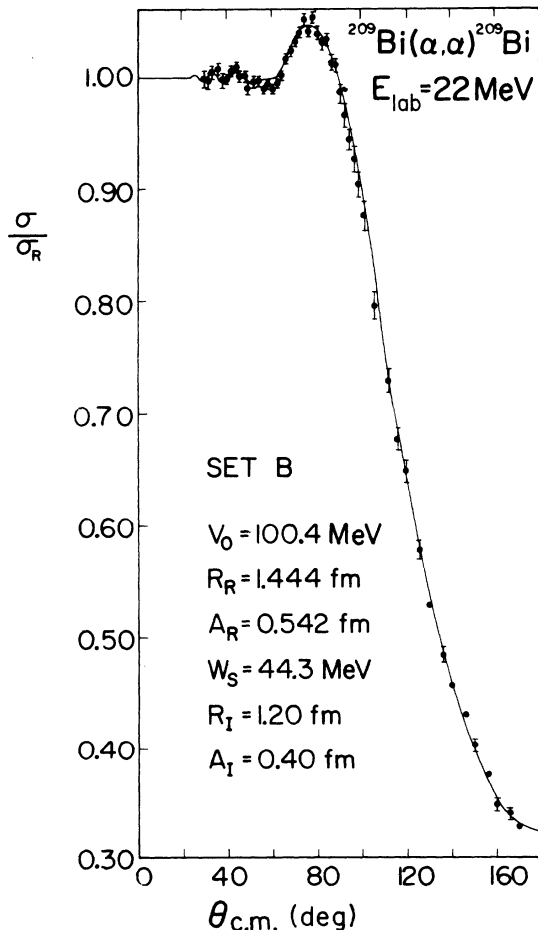


FIG. 2. Precision measurements of the elastic angular distribution, relative to Rutherford, of 22-MeV α particles scattered by ^{209}Bi . The solid curve is an optical-model fit with the parameters: Set B.

using an experimental arrangement similar to the one described above.

Four detectors, each separated by 10° as before, were used to cover the angular range between 30 and 100° in the laboratory system.

Pulse pileup was reduced by using Ortec 109A preamplifiers followed by Canberra 1416 post amplifiers. A pulse generator, triggered by the beam-current-integrator output pulse and fed through the electronics system furnished an accurate measure of the dead time, which was never greater than 2%. The target ($100\text{-}\mu\text{g}/\text{cm}^2$ ^{209}Bi on a $10\text{-}\mu\text{g}/\text{cm}^2$ carbon backing) was set with its normal at 40° to the incident beam for all measurements. Great care was taken with the beam transport and with detector aperture construction; as a result, no background subtraction at all was required.

Fixed detectors at 30° to the left and right of the incident beam monitored the horizontal beam position on the target. The summed count in the two monitor detectors was used to normalize the data. This was checked also against the current integrator and confirmed that there was no target deterioration during the experiment. The zero angle of the ring was checked by taking several left-right measurements.

Multiple overlaps of data taken independently by the four detectors at the same angles enabled an accurate set of ratios to be determined between the detector solid angles, and hence, a precise relative angular distribution over the entire angular range was obtained. This distribution was normalized by requiring that the weighted mean of

TABLE I. Reaction channels for α particles incident on ^{208}Pb and ^{209}Bi .

Reaction	Q value (MeV)	$\tau_{1/2}$	E_α (MeV)
^{208}Pb target			
$(\alpha, \gamma)^{212}\text{Po}$	-8.95	0.30 μsec ; 45 sec	8.79; 11.65
$(\alpha, n)^{211}\text{Po}$	-14.97	0.52 sec, 25 sec	7.45, 7.30
$(\alpha, p)^{211}\text{Bi}$	-14.78	2.14 min	6.6, 6.3
$(\alpha, 2n)^{210}\text{Po}$	-19.52	138.4 day	5.31
$(\alpha, d)^{210}\text{Bi}$	-17.67	5.01 day; 3×10^6 yr	4.65, 4.96
$(\alpha, t)^{208}\text{Bi}$	-16.01	$> 2 \times 10^{18}$ yr	...
$(\alpha, ^3\text{He})^{209}\text{Pb}$	-16.63	3.3 h	0.64(β^-)
^{209}Bi target			
$(\alpha, \gamma)^{213}\text{At}$	-9.37	$< 1 \mu\text{sec}$	9.07
$(\alpha, n)^{212}\text{At}$	-15.26	0.31 sec; 0.12 sec	7.66; 7.82
$(\alpha, p)^{212}\text{Po}$	-12.76	0.30 μsec , 45 sec	8.79; 11.65
$(\alpha, 2n)^{211}\text{At}$	-20.34	7.2 h	5.88
$(\alpha, d)^{211}\text{Po}$	-16.55	0.52 sec, 25 sec	7.45; 7.30
$(\alpha, t)^{210}\text{Po}$	-14.84	138.4 day	5.31
$(\alpha, ^3\text{He})^{210}\text{Bi}$	-15.98	5.01 day; 3×10^6 yr	4.65; 4.96

16 angles between 30 and 60° agree with Rutherford scattering. Optical-model calculations suggest that this procedure should be accurate to approximately 0.1%. The previous 22-MeV data (most forward angle 65°) were reduced by 1.7% in order to renormalize them to these more accurate data.

The final combined distribution is given in Fig. 2. The relative errors, which are 0.5–1.0% for $\Theta \leq 100^\circ$, and 1.5% for $\Theta > 100^\circ$, include effects due to statistics, normalization, and angular uncertainties.

B. Reaction cross-section measurements

The α -induced reaction channels on ^{208}Pb and ^{209}Bi were observed by detecting the decay products of the residual nuclei. Table I lists the Q value, particle energy, and half-life for several possible reactions below the $(\alpha, 2n)$ thresholds. Of these, only (α, n) is likely to be important, except possibly for (α, γ) near the (α, n) threshold, since the charged-particle Coulomb barrier drastically inhibits the other possible reaction channels.

The induced α activities were determined using two independent methods. In the first, the decay α particles were observed in the energy spectrum of scattered α particles, and the reaction cross section compared directly with elastic scattering. The second was a pulsed-beam measurement which allowed accurate relative measurements to be taken down to low energies.

1. Absolute measurements of (α, n) cross sections

The experimental arrangement was similar to that used in the elastic scattering measurements described above.

The induced activities are quite small and great care was taken to obtain clean energy spectra. Specially constructed rectangular nickel slits in front of each detector were carefully cleaned and polished to minimize edge scattering associated with the intense elastic peak. The collimator thickness was chosen to be 30% greater than the maximum α -particle range. A measure of the improvement achieved can be seen by comparing Fig. 3 with Fig. 1 of Ref. 2, which is also a spectrum at 19 MeV. (Note that the 0.1% tail extending 1 MeV below the elastic peaks of Ref. 2 has been eliminated here by the use of improved preamplifiers with pole zero compensation.) The background was reduced further by defining the incident beam far from the scattering chamber at a cross over between the two quadrupoles in the beam line, and using only clean-up apertures at the chamber entrance.

Energy spectra at 18, 19, 20 and 22 MeV were taken at several angles in the backward hemi-

sphere. The lower energies naturally have a relatively larger background correction, and the final normalization of the relative data described below was made to the results at 20 and 22 MeV near the maxima in the (α, n) excitation functions.

As shown in Fig. 3 the α -activity peaks are clearly identifiable in the prompt spectrum of scattered particles. Their energies correspond to the known α -decay energies (see Fig. 4), their angular distributions are isotropic, and they exhibit no kinematic shift with either bombarding energy or scattering angle. The summed counts in the observed peaks correspond to the major α groups which are known to constitute 98% of the total decays, and a simple correction was made to include those peaks which could not be seen above the background.

No conclusive evidence was found in any of the spectra for either the (α, γ) or the (α, p) reactions, and none was expected. However, radiative capture may begin to compete near the neutron threshold, where statistical considerations in heavy nuclei greatly enhance the nuclear lifetime with respect to neutron emission. For ^{208}Pb , an upper limit of 10% was established for the ratio $\sigma(\alpha, \gamma)/\sigma(\alpha, n)$ at 18 MeV, the lowest energy studied using this method. The figure for ^{209}Bi is somewhat less accurate owing to the presence of several trace contaminant peaks near the expected ^{213}At (g.s.) decay energy. At 19 MeV the ratio is less than 8% for bismuth and 2% for lead and, at 20 MeV the upper limits are 1 and 0.5%, respectively.

The elastic scattering peak was recorded at the same time as the activation products and $\sigma(\alpha, n)$ was determined directly via the elastic cross section, which was determined in the same experiment to an accuracy of a few percent.

The reproducibility of the results for different

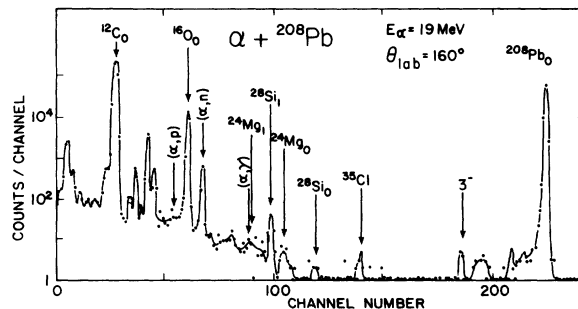


FIG. 3. Energy spectrum of 19-MeV α particles scattered by a ^{208}Pb target at 160° (lab). The peak marked (α, n) corresponds to the α decay of ^{211}Po . The α -decay energies of ^{212}Po and ^{211}Bi , following the (α, γ) and (α, p) reactions, also are indicated together with various contaminant peaks.

target thicknesses and backings was considered carefully, since it was essential to ensure that all the activated nuclei remained in the target. Carbon-backed lead and bismuth targets varying in thickness by a factor of 5 gave values of $\sigma(\alpha, n)$ which agreed within experimental error, after a correction was made for the small energy loss of the beam in the target. Unbacked targets gave poor agreement, the results indicating that 50–80% of the residual nuclei recoiled out of an unbacked 100- $\mu\text{g}/\text{cm}^2$ target. This explains the uniformly low results at 19, 18, and 17.5 MeV on ^{208}Pb quoted in Barnett and Phillips,² who commented on this possibility of escaping recoils.

2. Absolute $(\alpha, 2n)$ data

The thresholds for the reactions $^{208}\text{Pb}(\alpha, 2n)^{210}\text{Po}$ and $^{209}\text{Bi}(\alpha, 2n)^{211}\text{At}$ are at bombarding energies of 19.9 and 20.7 MeV, and these reactions are important contributors to the total reaction cross section at 22 MeV. The half-lives of the residual nuclei of 138 day and 7.2 h, respectively, make them suitable for chemical separation, and it was using this method that the Bi cross section was measured by Ramler *et al.*⁴ We measured the $^{209}\text{Bi}(\alpha, 2n)$ cross section at $E_\alpha = 22$ MeV and obtained a value of 66 ± 7 mb, in agreement with the (interpolated) values of Ref. 4 and the more approximate values of Kelly and Segré.⁵ The fact that we have no value for $\sigma(\alpha, 2n)$ on ^{208}Pb means that we were unable to use the total reaction cross section at 22 MeV in the global fits (Sec. III).

3. Pulsed-beam measurement of relative (α, n) cross sections

Accurate relative (α, n) data between 16- and 24-MeV incident energy were obtained by chopping the incident beam and detecting the activity of the residual nuclei ^{212}At and ^{211}Po out of beam. The decay schemes are given in Fig. 4. This procedure eliminated the prompt background and the detectors could be placed very close to the target. The resulting increase in solid angle allowed measurements to be made well below the Coulomb barrier and towards the neutron thresholds.

A ladder of carbon-backed targets of ^{208}Pb and ^{209}Bi , varying in thickness between 100 and 600 $\mu\text{g}/\text{cm}^2$, was mounted on the target rod of the Ortec scattering chamber. This rod was attached to a pneumatically operated piston which could accurately and reproducibly move the ladder 2.5 cm vertically in approximately 0.1 sec. In the vacuum of the scattering chamber even the thinnest targets used could be moved safely in this way, and none was ever broken, even after 10^3

cycles.

Two 100- μm -thick surface-barrier detectors were placed facing each other on opposite sides of the target ladder and 2.5 cm below the beam line. Each detector, set 0.5 cm from the target axis, subtended a solid angle of approximately 0.5 sr and was shielded in such a way that essentially none of the intense scattered beam reached it during the bombardment with the target in the "up" position.

The detectors were connected to a common pre-amplifier-amplifier chain and signals were fed via an ADC to the on-line CDC 3100 computer.

Each bombardment and detection cycle was controlled by the computer using a general purpose on-line "activity" routine ACT.⁶ The sequence of operations was as follows:

- (1) The target, in the upper position, was bombarded for a predetermined period (typically 2 sec). The time distribution of the beam during this time was recorded by storing the digital beam-current information in 128 slots into which the bombardment time was divided.
- (2) A signal from the computer closed a beam Faraday cup located just beyond the accelerator energy control slits. This operation occurred in a time which was short compared with the half-lives being measured.
- (3) After a delay of approximately 0.1 sec, the computer triggered the target rod piston and the target was moved between the two detectors.
- (4) After a further short delay, the energy spectra of the decay α particles above 5 MeV were recorded in complete freedom from background for a specified period of several half-lives. This period was subdivided into 32 time slots. During each one, the data were stored in a separate 128 channel array. Time slots were 200-msec duration for the polonium activity and 100 msec for the astatine activity. For completeness, several runs were taken with 2-sec time slots and a 64-sec bombardment time to emphasize the $^{211}\text{Po}^m$ decay.

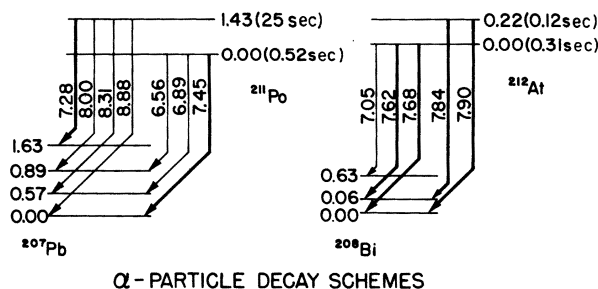


FIG. 4. α -particle decay schemes of ^{211}Po and ^{212}At , formed by the (α, n) reaction on ^{208}Pb and ^{209}Bi .

(5) Finally, the counters were disabled, the target rod raised again, and the entire cycle repeated until sufficient statistics were obtained.

4. Results and analysis of half-lives and cross sections

The energy spectra of the α activities resulting from the (α, n) and $(\alpha, 2n)$ reactions on ^{208}Pb and ^{209}Bi at 22 MeV are shown in Fig. 5. The peaks are labeled and correspond to the emitted α particles indicated in the decay schemes shown in Fig. 4 for ^{211}Po and ^{212}At . In this particular example, the bombarding energy is above the $(\alpha, 2n)$ thresholds of both target nuclei, and decays associated with the residual nuclei ^{210}Po and ^{211}At also appear. Their half-lives, however, are much too long for the cross section $\sigma(\alpha, 2n)$ to be determined using the present method.

Regions of the energy spectra of Fig. 5 could be selected to contain either the ground-state isomer or the metastable isomer free from other contaminants. The decay curves for each activity (Fig. 6) were extracted from the data and analyzed using a nonlinear least-squares routine EXPFIT.⁶

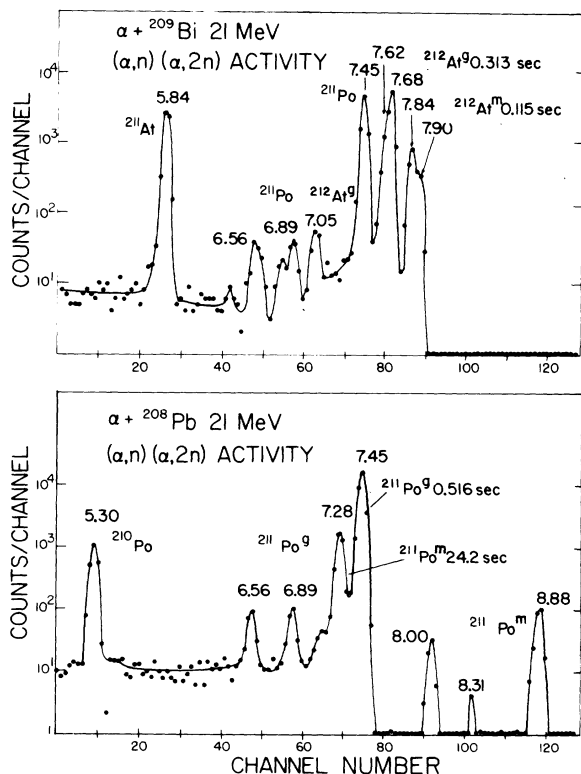


FIG. 5. Energy spectra of α particles emitted by ^{208}Pb and ^{209}Bi targets immediately after bombardment with 21-MeV α particles. All peaks correspond to the decay products of nuclei formed in either the (α, n) or $(\alpha, 2n)$ reactions.

The results of weighted fits to all the data are given in Table II. Various checks were made during the experiment, e.g., by varying the waiting period before accumulating the data and by analyzing different portions of the decay curves. The results are consistent with the errors quoted, which are statistical only. About 30 measurements were made on each half-life. The time scale was derived from the 10-MHz crystal oscillator in the CDC 3100 computer and is common to all results; its accuracy, is sufficiently high that it did not affect the errors in the final results.

A comparison with all other measurements is presented in Table II. Of the most accurate previous results for $^{211}\text{Po}^g$, the value of Tove⁷ is in

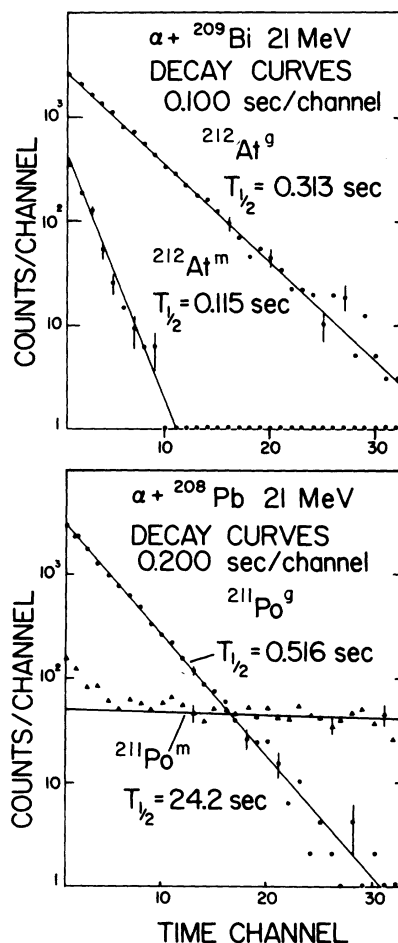


FIG. 6. Decay curves showing the half-lives of α peaks shown in Fig. 5. The upper curves show the 0.313-sec half-life of the 7.62- and 7.68-MeV α decays of the ground state of ^{212}At , and the 0.115-sec 7.84- and 7.90-MeV α decays of the 0.22-MeV metastable state of ^{212}At . The lower curves show the 0.516-sec decay of the 7.45-MeV peak due to the ground-state decay of ^{211}Po , and the 24.2-sec decay of the 7.28-MeV α peak from the 1.43-MeV metastable state of ^{211}Po .

TABLE II. Half-lives (sec) of $^{211}\text{Po}^g$, $^{211}\text{Po}^m$, $^{212}\text{At}^g$, and $^{212}\text{At}^m$.

Isomer	$^{211}\text{Po}^g$	$^{211}\text{Po}^m$	$^{212}\text{At}^g$	$^{212}\text{At}^m$
Present work	0.516 ± 0.003	24.2 ± 0.5	0.313 ± 0.003	0.115 ± 0.002
	0.56 ± 0.04^a	25.5 ± 0.3^b	0.315 ± 0.003^c	0.122 ± 0.001^c
	0.52^d	25^d	0.305^d	0.122^d
	0.5 ± 0.1^e	27 ± 5^e		
		25 ± 2^f		
Best values (weighted mean)	0.516 ± 0.003	25.2 ± 0.5	0.314 ± 0.002	0.121 ± 0.005

^a Reference 7.

^b I. Perlman, F. Asaro, A. Giorso, A. Larsh, and R. Latimer, Ref. 8.

^c Reference 9.

^d W. B. Jones, Phys. Rev. **130**, 2042 (1963). No error given.

^e M. M. Winn, Proc. Phys. Soc. **67A**, 949 (1954).

^f V. A. Karnaukhov, Zh. Eksp. Teor. Fiz. **42**, 973 (1962) [transl.: Sov. Phys.—JETP **15**, 671 (1962)].

good agreement; for $^{211}\text{Po}^m$, Perlman *et al.*⁸ quote 25.5 ± 0.3 sec which is a little higher than our value; and of the two results for the astatine isotopes from Reeder,⁹ that for $^{212}\text{At}^g$ agrees well, while the other for $^{212}\text{At}^m$ is significantly different. We can find no reason for this disagreement. Suggested best values for the four activities are included in Table II. They are: $^{212}\text{Po}^g$ 0.516 ± 0.003 sec; $^{211}\text{Po}^m$ 25.2 ± 0.5 sec; $^{212}\text{At}^g$ 0.314 ± 0.002 sec; and $^{212}\text{At}^m$ 0.121 ± 0.005 sec.

Using our half-life values, and the time distribution of the beam during the bombardment cycle, the total recorded activity was corrected to give a number proportional to the total induced activity and thus to the (α, n) cross section. In general, α particles emitted from the ground and meta-stable states were easily resolved (Fig. 5) and no error resulted from peak overlap. The ground-state activities were determined with good statistics and, since the time between bombardment and counting was less than the half-life in each case, little additional error was introduced due to the errors in the half-lives. In the case of $^{212}\text{At}^m$ ($\tau_{1/2} = 0.115$ sec) a large fraction of the induced activity decayed in the interval between beam off and the start of the counting period, and even though a thick target was used below 18 MeV, the $^{212}\text{At}^m$ activity was determined with rather poor statistics. This uncertainty was the biggest contribution to the error in the $^{209}\text{Bi}(\alpha, n)$ data at the lowest energies.

Only an upper limit to the $^{211}\text{Po}^m$ activity could be obtained below 19 MeV. However, because of its relatively long half-life (25 sec) this activity could be detected efficiently and was shown to

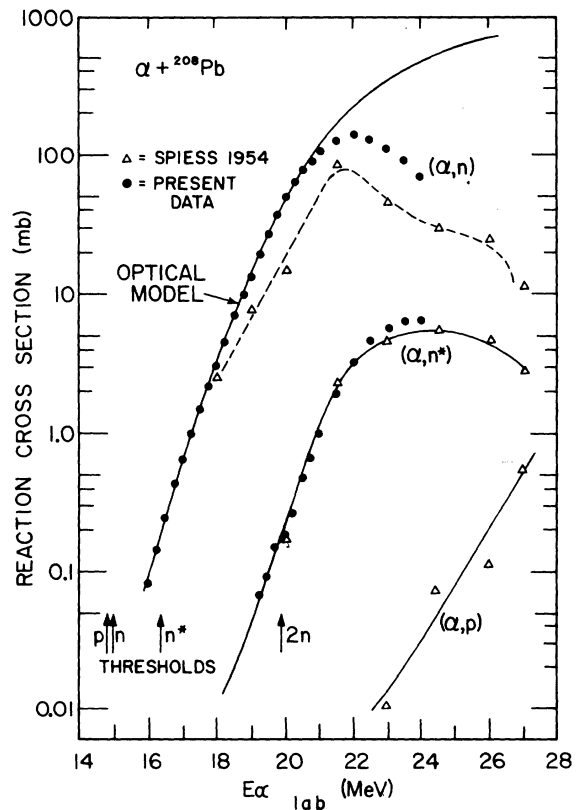


FIG. 7. Reaction cross-section data summary for α particles incident on ^{208}Pb . The solid circles represent the present data for $^{208}\text{Pb}(\alpha, n)^{211}\text{Po}$ (ground state) and the $^{208}\text{Pb}(\alpha, n^*)^{211}\text{Po}$ (metastable state). The triangles show the data of Ref. 10 for the above reactions and also for the (α, p) reaction. Energy thresholds for the (α, p) , (α, n) , (α, n^*) , and $(\alpha, 2n)$ reactions also are shown.

contribute a negligible amount to the total $^{208}\text{Pb}(\alpha, n)$ cross section at all but the highest energies (Fig. 7 and Table III).

The final relative (α, n) data were normalized to the 20- and 22-MeV absolute measurements described above. The over-all errors range from 5 to 45%. Table III contains the values of the cross sections we measured.

Figure 7 contains a summary of all existing data for the α -induced reaction cross sections on ^{208}Pb between 15 and 28 MeV; curiously, the $(\alpha, 2n)$ cross section is not known. The data are from Spiess¹⁰ for the $^{208}\text{Pb}(\alpha, n)^{211}\text{Po}^g$, $^{208}\text{Pb}(\alpha, n^*)^{211}\text{Po}^m$, and $^{208}\text{Pb}(\alpha, p)^{211}\text{Bi}$ reactions, and in the region of overlap the agreement is better than a factor of 2. The fission cross section is negligible, being only $50 \mu\text{b}$ at 28 MeV.¹¹

In Fig. 8 we plot the current situation for ^{209}Bi as a target. The data of Ramler *et al.*⁴ for the $^{209}\text{Bi}(\alpha, 2n)^{211}\text{At}$ and $^{209}\text{Bi}(\alpha, 3n)^{210}\text{At}$ reactions in the energy range 20.6–43.3 MeV supersedes the

earlier work of Kelly and Segré.⁵ Both these groups used the stacked-foil technique and radiochemical separation. Their cross sections refer to the detected residual nucleus and the reaction which produced it is inferred. Chulick and Natowitz¹² have measured the $^{209}\text{Bi}(\alpha, pn)^{211}\text{Po}$ and the $^{209}\text{Bi}(\alpha, p)^{212}\text{Po}$ reaction cross sections, again by activity measurements, and at 30.5 MeV the results are $33 \mu\text{b}$ ($^{212}\text{Po}^m$), $\sim 0.8 \text{ mb}$ ($^{212}\text{Po}^g$), and 0.10 mb ($^{211}\text{Po}^m$). We therefore expect a negligible contribution at 22 MeV to the total reaction cross section. The fission cross section has been measured by Huizenga, Chaudhry, and Vandenbosch¹¹ and by Halpern and Nicholson¹¹; while it is considerably larger than for ^{208}Pb it amounts to only $1 \mu\text{b}$ at 20 MeV and nearly 1 mb at 28 MeV.

The separate cross sections for the reactions $^{209}\text{Bi}(\alpha, n)^{212}\text{At}^g$ (0.316 sec) and $^{209}\text{Bi}(\alpha, n^*)^{212}\text{At}^m$ (0.116 sec) which we measured are plotted in Fig. 9. The curve through the sum of the (α, n) data is the optical-model best fit. The isomer ratio

TABLE III. Total cross sections in mb for (α, n) reactions on ^{208}Pb and ^{209}Bi . Percentage errors are given in parentheses, and include an over-all 4% uncertainty from normalizing the relative data to absolute measurements at 20 and 22 MeV.

E_α (MeV)	$^{208}\text{Pb}(\alpha, n)^{211}\text{Po}^g$	$^{208}\text{Pb}(\alpha, n^*)^{211}\text{Po}^m$	$^{209}\text{Bi}(\alpha, n)^{212}\text{At}^g$	$^{209}\text{Bi}(\alpha, n^*)^{212}\text{At}^m$
24.0	69.9 (6)	6.5 (10)	28.2 (5)	63.4 (5)
23.5	89.9 (6)	6.4 (10)	39.0 (5)	76.5 (5)
23.0	112.0 (6)	5.6 (10)	52.0 (5)	80.7 (5)
22.5	127.1 (6)	4.5 (10)	65.1 (5)	77.8 (5)
22.0	134.9 (5)	3.2 (6)	75.7 (5)	68.0 (5)
21.5	124.7 (5)	1.9 (6)	78.6 (5)	54.5 (5)
21.25			73.7 (5)	47.8 (5)
21.0	102.8 (5)	1.0 (6)	66.8 (5)	37.1 (5)
20.75	89.0 (5)	0.67 (7)	57.3 (5)	30.7 (5)
20.5	76.7 (5)	0.48 (7)	49.4 (5)	23.0 (5)
20.25	64.8 (5)	0.26 (8)	37.9 (5)	16.1 (5)
20.0	49.1 (5)	0.18 (7)	27.5 (5)	12.3 (5)
19.75	36.9 (5)	0.145 (9)	21.8 (5)	7.8 (6)
19.5	26.7 (6)	0.089 (11)	15.6 (5)	7.07 (6)
19.25	19.2 (6)	0.066 (11)	11.29 (5)	4.84 (8)
19.0	13.64 (6)		7.55 (5)	3.53 (5)
18.75	9.73 (6)		5.43 (5)	2.46 (8)
18.5	7.13 (6)		3.58 (5)	0.99 (11)
18.25	4.45 (6)			
18.0	3.00 (10)		1.60 (5)	0.65 (8)
17.75	2.05 (10)			
17.5	1.42 (10)		0.74 (6)	0.38 (15)
17.25	0.96 (10)			
17.0	0.601 (10)		0.295 (5)	0.101 (13)
16.75	0.400 (10)			
16.5	0.235 (10)		0.121 (6)	0.027 (22)
16.25	0.133 (10)		0.066 (7)	0.019 (40)
16.0	0.078 (10)		0.039 (7)	0.005 (45)

σ_m/σ_g is also plotted on the figure. No attempt has been made to fit this curve or the individual (α, n) cross sections.

III. OPTICAL-MODEL ANALYSIS

The optical-model analysis of the combined elastic scattering and reaction cross-section data was done in two stages. A global analysis was carried out including, eventually, all the elastic scattering data for both nuclei. The results of this lead to the second part in which the precision 22-MeV ^{209}Bi data were fitted. Here, a much more exhaustive exploration of parameter space was undertaken and a variety of acceptable potentials were then compared with the lower-energy data. Some details of these analyses are given below.

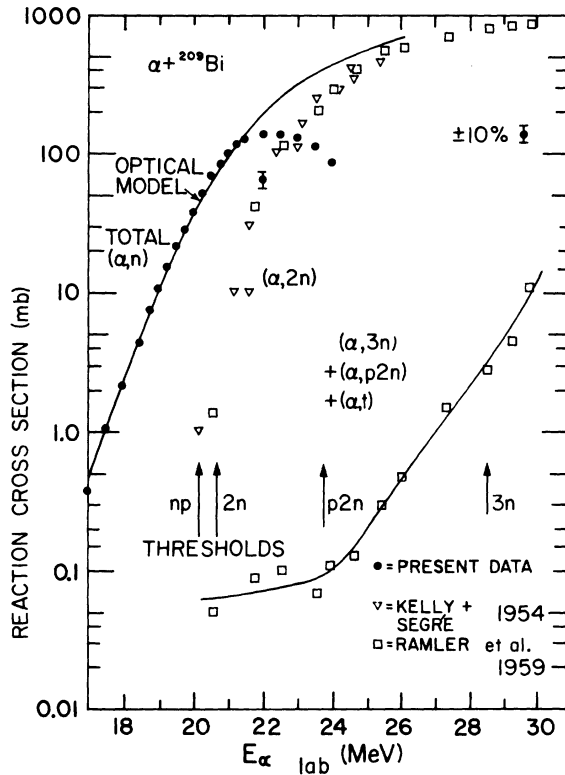


FIG. 8. Summary of the α -induced reaction cross-section data for ^{209}Bi as a function of energy. Present (α, n) data [and one $(\alpha, 2n)$ data point] are indicated by the solid circles. The solid curve was obtained from an optical-model fit to these and the elastic scattering data shown in Fig. 1. The $(\alpha, 2n)$ data of Ref. 5 are indicated by the inverted triangles. The squares are the data of Ref. 4 for the $(\alpha, 2n)$ reaction and, at the lower right, for the combined (α, t) , $(\alpha, p2n)$, and $(\alpha, 3n)$ reactions. The solid curve through the latter points is not a fit. (α, np) , $(\alpha, 2n)$, $(\alpha, p2n)$, and $(\alpha, 3n)$ energy thresholds are indicated.

A. Global analysis

Data for both ^{208}Pb and ^{209}Bi at different energies were fitted simultaneously with an energy-independent optical model using different geometries for the real and imaginary potentials. This was done using the global search routine BOMB¹³ which minimizes the quantity

$$\chi^2 = \sum_N [\chi^2_{\theta}/n + \chi^2_R],$$

$$\chi^2_{\theta} = \sum_n \{ \sigma_{\text{exp}}(\Theta) - \sigma_{\text{th}}(\Theta) \}^2 / \Delta\sigma^2, \quad (1)$$

where χ^2_{θ} and χ^2_R are calculated from the angular distribution and reaction cross section at a given energy, N is the number of data sets, and n is the number of points in the angular distribution. To avoid overemphasizing the reaction cross-section measurements in computing χ^2 via Eq. (1), errors in σ_R values were taken to be $\pm 10\%$, rather

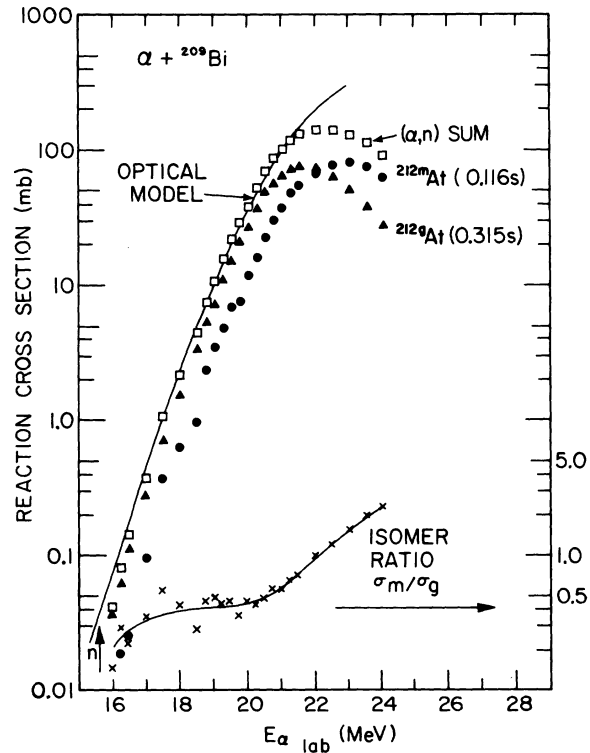


FIG. 9. Summary of the present measurements of the $^{209}\text{Bi}(\alpha, n)^{212}\text{At}$ reaction. The triangles and circles, respectively, show the cross section to the ground state and 0.22-MeV metastable state of ^{212}At . The ratio of these cross sections is shown at the bottom of the figure. The total measured (α, n) cross section is shown by the squares. The solid curve is the same optical-model fit shown in Fig. 8. The arrow indicates the (α, n) threshold.

than the actual values quoted in Table III.

The optical-model potential describing the nuclear interaction was of the standard form:

$$U(r) = V_0 f(r, R_R, a_R) + iW_0 g(r, R_I, a_I), \quad (2)$$

where $f(r)$ is the regular Woods-Saxon form factor and $g(r)$ is either Woods-Saxon for volume absorption or the derivative form: $4a_I f'(r, R_I, a_I)$, for surface absorption. The Coulomb potential was taken to be that due to a uniformly charged sphere of radius $R = 1.2A^{1/3}$ fm.

Data sets consisted initially of angular distributions for both nuclei at 19, 20, and 22 MeV, plus reaction cross-section data on ^{209}Bi at these energies and on ^{208}Pb at 19 and 20 MeV. The 22-MeV reaction data on ^{208}Pb were excluded because the $(\alpha, 2n)$ contribution, which is important at this energy, is not known. For the $\text{Bi}(\alpha, 2n)$ reaction our value of 66 ± 7 mb (Sec. IIB2) was used for the cross section at 22 MeV.

Although it was possible to minimize χ^2 by varying all six potential parameters simultaneously using a pattern search,¹³ in practice, because of the presence of ambiguities to be described later, this was not a fruitful procedure. A method which was consistently successful was to perform limited searches on subsets of the parameters followed by a fine mesh search on V and W . The

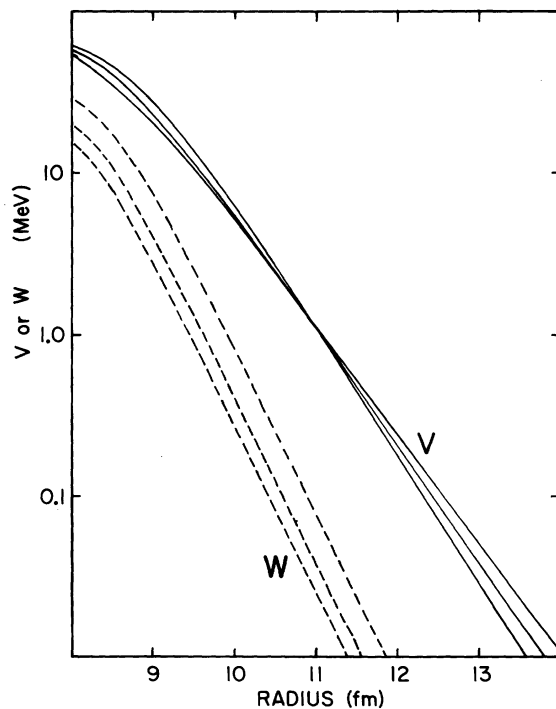


FIG. 10. Several real and imaginary surface form factors which give acceptable global fits to all the α - ^{208}Pb and α - ^{209}Bi scattering and reaction data.

program automatically searches for the optimum normalization change for each angular distribution within preset limits, which, in this case, were $\pm 3\%$. In no case did the final normalization change exceed 1.5%.

Different sets of starting parameters were tried together with different search patterns, in order to try to avoid any bias in the way the final converged set of parameters was approached.

In this manner good fits were obtained for several different sets of optical parameters. Figure 1 compares the elastic scattering data with predictions using one of the parameter sets. In general, although a good compromise was achieved in this analysis, it was not possible to obtain optimum fits to both the 22-MeV scattering data and the 19-MeV reaction cross-section data simultaneously. About 50% of the total contribution to χ^2 was due to the 22-MeV elastic and the 19-MeV reaction cross-section data, due to the weighting chosen in Eq. (1).

These early results showed, perhaps unexpectedly, that even with the reaction data included the fits are quite insensitive to any features of the

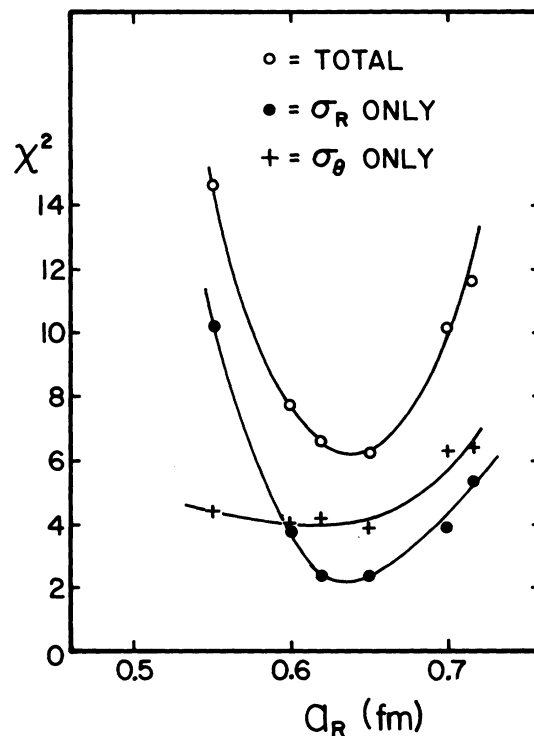


FIG. 11. The dependence of χ^2 , obtained in the global analysis, on the real diffuseness parameter, a_R . χ^2 [given by Eq. (1)] measures the over-all quality of fit to the scattering and reaction data (open circles), the reaction data alone (solid circles), and the scattering data alone (crosses).

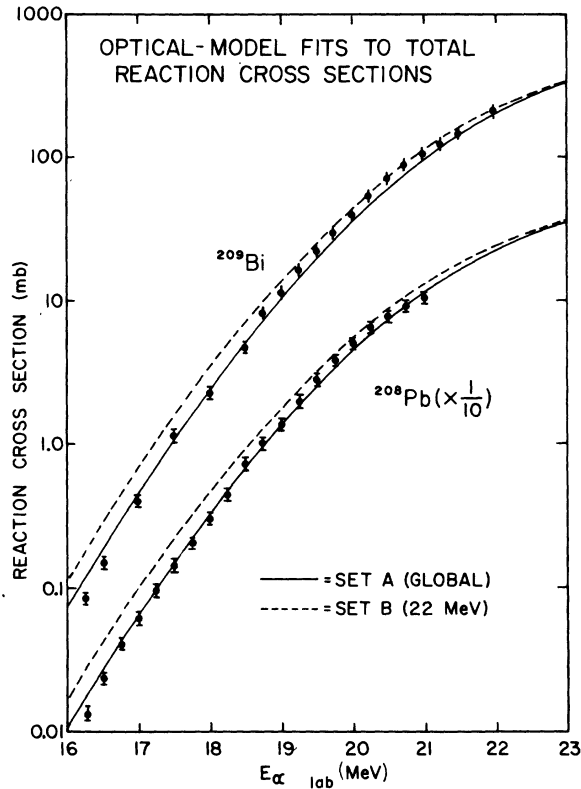


FIG. 12. Optical-model fits to the α -induced total reaction cross-section data on ^{209}Bi and ^{208}Pb . The solid curves are given by the parameters of Set A (Fig. 1), and represent one of the best global fits to all the elastic and reaction cross-section data. The dotted curves are given by the parameters of Set B (Fig. 2) which represent one of the best fits to the 22-MeV α - ^{209}Bi scattering and reaction cross-section data.

absorptive potential. Acceptable parameter sets could be found using either a volume or surface form for W , which varied in magnitude over a wide range.

The real central strength V_0 was also poorly

defined, confirming the well-known insensitivity to the nuclear interior. Moreover, also in agreement with other studies of α scattering,^{1,14} V_0 and R_R are correlated in a way which reproduces the real potential at large radii.

Real and imaginary potential form factors at large radii, corresponding to acceptable fits for different values of the real diffuseness a_R , are shown in Fig. 10. It is clear that, at these low bombarding energies, the value of the real potential near 11 fm is a well determined quantity. This point lies about 3 fm beyond the half-way radius of the nuclear potential and corresponds to the peak of the real potential barrier for an $l=0$ α particle on these nuclei. This radius will be denoted by r_{max} . It is not surprising that the strong absorption radius¹⁵ also occurs near 11 fm showing that the real potential is most accurately determined where the interaction is most important.

The real diffuseness parameter a_R is the only single parameter to which the fits were at all sensitive. The results of a grid search on a_R are shown in Fig. 11. Open circles show values of χ^2 for a simultaneous fit to all the data considered on both target nuclei. It is clear that the sensitivity to a_R is due mainly to the reaction cross-section contribution (solid circles), and that the scattering data alone (crosses) are relatively insensitive to this parameter.¹⁶

These best-fit potential parameters were not changed significantly when the more extensive (α, n) data were included in the analysis. In Fig. 12 we plot the total reaction cross-section data for both nuclei. The solid curves in Fig. 12 are given by potential Set A (Fig. 1) which gave one of the best global fits to all the data between 19 and 22 MeV. The agreement with the new data is quite remarkable and continues in the region below 19 MeV which was not considered in the earlier analysis. This suggests that the Set A potential

TABLE IV. Some equivalent potentials obtained from the 22-MeV $\alpha + ^{209}\text{Bi}$ analysis.

V_R (MeV)	110.9	200.2	100.4	159.7	86.89	35.00	90.29	92.5	94.62	117.51
R_R (fm)	1.464	1.390	1.444	1.387	1.449	1.518	1.411	1.384	1.364	1.298
a_R (fm)	0.50	0.529	0.542	0.560	0.55	0.571	0.60	0.625	0.65	0.70
W_V (MeV)					7.92		62.73			
W_S (MeV)	132.2	152.1	44.3	50.4		17.78		30.5	21.0	21.6
R_I (fm)	0.779	1.216	1.200	1.216	1.358	1.304	1.358	1.216	1.285	1.270
a_I (fm)	0.206	0.183	0.400	0.432	0.484	0.545	0.482	0.572	0.561	0.591
$V_{(11 \text{ fm})}$ (MeV)	1.08	1.10	1.12	1.12	1.10	1.04	1.12	1.06	1.07	1.05
$W_{(11 \text{ fm})}$ (MeV)	0.000	0.000	0.011	0.032	0.018	0.178	0.140	0.163	0.204	0.244
$\langle r^2 \rangle_R^{1/2}$ (fm)	6.981	6.687	6.936	6.704	6.969	7.293	6.857	6.772	6.717	6.509
J_R (MeV fm ³)	376.1	586.5	329.1	466.1	288.2	133.3	278.9	271.5	267.2	291.1
$\sigma_{\text{react}}(17 \text{ MeV})$ (mb)	0.694	0.679	0.702	0.712	0.682	1.169	0.923	1.182	1.285	1.590
$\sigma_{\text{react}}(22 \text{ MeV})$ (mb)	217.5	214.0	215.9	213.6	212.3	218.0	212.5	211.8	211.6	210.5

would serve well in calculations of the absolute α -decay rate from radioactive nuclei. That these rates are in gross disagreement with experiment has been attributed¹⁷ to the fact that the α -nucleus potential used in the calculations is one determined far above the Coulomb barrier (mostly at 40 MeV). We recognize in the energy dependence of the total reaction cross section (Fig. 12) the direct influence of the α -particle barrier. Our experiment, in many respects, is simply the inverse of α decay and so the potentials we obtain are expected to be very relevant to the α -decay calculations.

B. Analysis of the 22-MeV ^{209}Bi data

The dotted curves in Fig. 12 are given by a potential (Set B, Fig. 2) which was obtained from an analysis of the accurate 22-MeV ^{209}Bi data, described below, and affirms the indications of the global analysis that a compromise had to be made between the higher- and lower-energy data. An optimum fit to the 22-MeV scattering data gave a rather poor fit to the lower-energy reaction data, and vice versa. There is no indication from studies at higher energies that the α -nucleus potential is energy-dependent. Moreover, an energy dependence similar to that found for α particles on nucleons^{18,19} is insignificant over the small energy range considered here, and would tend to enhance rather than diminish the discrepancy.

It was partly in order to investigate this discrepancy that the accurate 22-MeV ^{209}Bi results were taken. These measurements, together with the reaction cross section at this energy, proved to be much more difficult to fit than the

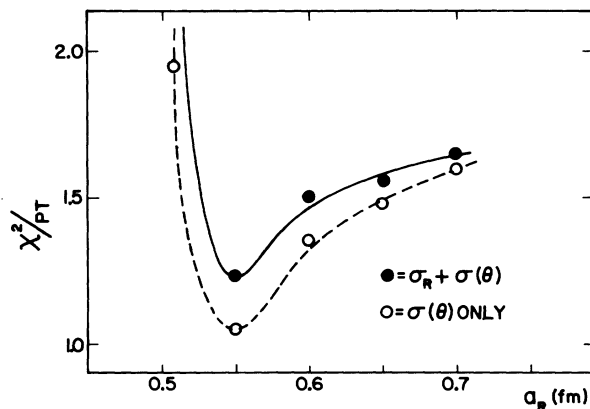


FIG. 13. The variation of χ^2 per point with the real diffuseness parameter a_R for optical-model fits to the accurate 22-MeV α - ^{209}Bi elastic scattering and reaction cross-section data (solid circles). The open circles are for fits to the scattering data alone.

earlier data with 2% errors, and a more complete scan of parameter space was undertaken to try to find an acceptable potential, which also would reproduce the reaction data at lower energies. The 22-MeV ^{209}Bi data were fitted using the computer code RAROMP.²⁰ The nuclear potential is given by Eq. (2).

An initial search indicated that the optimum normalization factor was less than 1.0025. No normalization was used in the subsequent fitting and χ^2 values per point close to unity were obtained for the best fits, an example of which is shown in Fig. 2. This represents a significant improvement of a factor of about 3 in the best fit to these data which was achieved in the global analysis.

A large number of acceptable potentials were found in the real parameter space of interest. A number of these are listed in Table IV, together with quantities which illustrate some of the results of the analysis. As expected, the main findings completely confirm those of the earlier global analysis. The interaction is sensitive to only the tail of the real potential $V(r)$ near $r_{\text{max}} = 11$ fm. Inside the nucleus, $V(r)$ is undetermined; indeed, a grid on the real central strength V_0 gave essentially identical fits for V_0 ranging between 35 and 250 MeV.

Careful analyses of α scattering on lighter nuclei have revealed a discrete ambiguity in V_0 , corresponding to wave functions with different numbers of nodes in the nuclear interior.²¹ This ambiguity was not detected in the present work, probably because the potential near the interaction

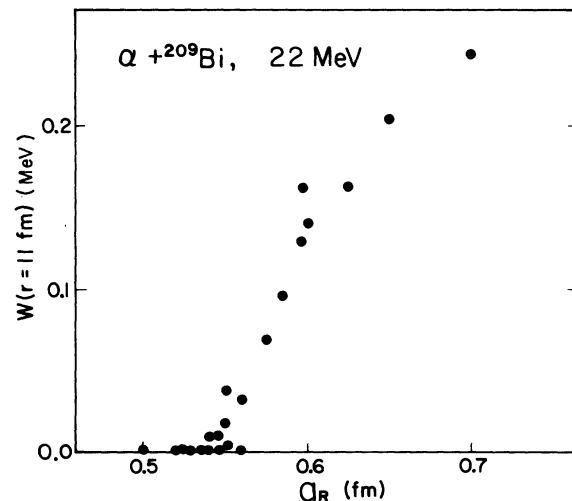


FIG. 14. The dependence of the imaginary potential evaluated at 11 fm as a function of the real diffuseness parameter a_R , for equivalent potentials obtained in the analysis of the 22-MeV α - ^{209}Bi data.

region is so small; and the discrete values are so close together (within 20 MeV) that adjustments to the shape of $V(r)$ and the compensating effects of the imaginary potential cause them to merge into a continuous ambiguity in V_0 .

It was not possible to grid on $V(r_{\max})$ explicitly. However, the values obtained from the many acceptable fits (see Table IV) give $V(r_{\max}) = 1.10 \pm 0.08$ MeV. The results of an a_R grid, shown in Fig. 13, show a rather broad asymmetrical minimum in χ^2 near $a_R = 0.55$ fm, using a volume form for $W(r)$. Similar findings, with essentially identical values for χ^2 , were obtained using a surface form for the imaginary potential.

The tail of the imaginary potential is considerably smaller than that of the real potential and, as a result, is less well known. In no case does its value near 11 fm exceed 0.25 MeV and the best fits indicate that it is less than 0.1 MeV. The real diffuseness a_R and $W(r_{\max})$ appear to be correlated; larger values of a_R correspond to larger values of $W(r_{\max})$. (See Fig. 14.) The surface fall off of the imaginary potential, represented by a_I , is rather poorly determined, but, in all cases, is smaller than that for real potential. It was not possible to obtain a good fit using equal real and imaginary geometries; the region of absorption must be inside the real potential.

Although the predicted reaction cross sections of the equivalent potentials (Table IV) are similar at 22 MeV, they differ considerably at lower en-

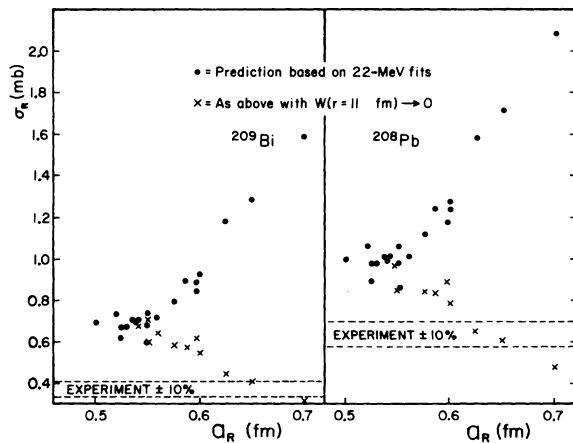


FIG. 15. The dependence on the real diffuseness parameter a_R of the α -induced total reaction cross section at 17 MeV for both ^{209}Bi and ^{208}Pb predicted using the "equivalent" potentials of the analysis of the 22-MeV α - ^{209}Bi data (solid circles). The crosses are similar calculations in which the value of the surface absorption potential at 11 fm was reduced to zero while maintaining a reasonable value in the interior. The experimental 17-MeV measurements with a $\pm 10\%$ error range are shown by the dotted lines.

ergies. At 17 MeV, for example, the calculated reaction cross-section values differ by over a factor of 2 in a way that depends on $W(r_{\max})$ or a_R (see Fig. 15). In principle, therefore, it should be possible to pin down the surface potential shape more closely by fitting the reaction cross-section data. Unfortunately (as is shown in Fig. 15), this does not appear to be the case here. At 17 MeV, the predicted values based on the 22-MeV potentials, are systematically higher for both ^{208}Pb and ^{209}Bi than the experimental $\sigma(\alpha, n)$ results by an amount which greatly exceeds the experimental errors. This result is consistent with that of the global analysis which found difficulty in fitting simultaneously the 19- and 22-MeV data. It suggests that either the nuclear potential is markedly energy-dependent, the form of the parametrization inadequate, or there is a significant contribution to the reaction cross section in addition to the (α, n) channel.

The reaction cross section below the barrier is quite sensitive to changes in the real nuclear potential; a change of about 35% in $V(r_{\max})$ or 30% in a_R reduces σ_R (at 17 MeV) by a factor of 2. However, over such a small energy range these changes imply a large energy dependence in the real potential for which there is no evidence at high energies. Figure 16 shows a plot of the magnitude of the real potential at $r = 11$ fm, given by optical-model analyses of α - ^{208}Pb elastic scattering taken at a number of bombarding energies. As indicated by the triangular point at 17 MeV,

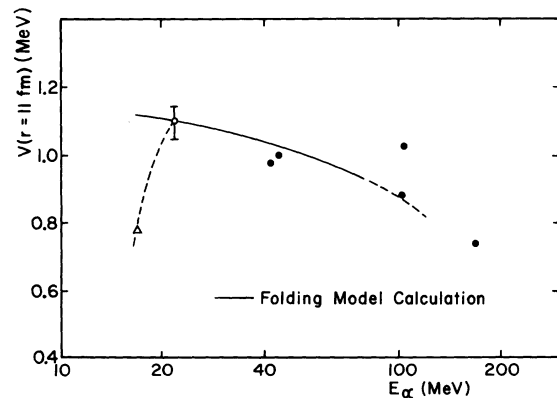


FIG. 16. The dependence of the real potential strength at 11 fm versus bombarding energy for α - ^{208}Pb . The open circle is given by the present analysis, the solid circles from previously published analyses. The solid curve is a prediction using the folding model as described in the text. The triangle indicates the value of $V(r = 11 \text{ fm})$ necessary to fit the measured reaction cross section at 17 MeV, if the absorption potential and real potential geometry are unchanged from the values obtained from analyzing data at 22 MeV.

a sharp drop is needed to fit the data at 17 MeV. This, as shown by the black dots, goes counter to the trend at higher energies where the surface potential is well described by a folding model, with an energy dependence given by that of a local α -nucleon potential.^{18,19}

On the other hand, there is considerable evidence for a strong energy dependence of the imaginary potential. Results for α scattering by ^{58}Ni , for which there are extensive data (e.g., Ref. 14) over a wide energy range, show that the absorption potential at low energies is considerably weaker and falls off more rapidly in the surface than that which is required to fit the higher-energy data.

The data are quite insensitive to the volume absorption and, as is clear from Fig. 15, only those potentials with large values of a_R will predict a significantly smaller σ_R if the surface absorption is decreased. The crosses in Fig. 15 show that, if $W(r_{\max})$ is reduced to zero, while maintaining the absorption in the nuclear interior, the reaction data at 17 MeV can be fitted with a real potential obtained from the 22-MeV analysis. However, the real diffuseness should be approximately 0.65 fm, which agrees with the indications of the earlier global analysis (see Fig. 11).

Alternatively, the experimental measurements may not account for all the reaction cross section. Simple penetrability arguments forbid any significant compound elastic scattering at 17 MeV, but the possibility of an (α, γ) contribution comparable with $\sigma(\alpha, n)$ cannot be ruled out completely for either target nucleus, since the very rapid decays of ^{213}At and ^{212}Po (each $< 1 \mu\text{sec}$) were not detected in the pulsed-beam experiment. The contribution would have to be relatively greater for ^{209}Bi , which is consistent with the higher neutron threshold for this target, although the absolute (α, γ) yields would be about the same for both targets.

Although no evidence for (α, γ) was seen in any of the direct energy spectra, the upper limits at 18 MeV (10% for ^{208}Pb and greater for ^{209}Bi) could account for at least part of the discrepancy. A measurement of (α, γ) at 16 or 17 MeV on either or both of these nuclei would help to clear up this uncertainty in the reaction cross section, and may allow even more definitive statements to be made about the α -nucleus potential.

C. Interaction potential

The results of the analysis described above clearly indicate that it is the real potential barrier which dominates the α interaction with lead

and bismuth at these energies and which controls the flux of α particles in and out to the target nucleus. The main role of the imaginary potential, at these low bombarding energies, is to prevent flux which has penetrated the real potential barrier from reemerging. There is very little sensitivity to the form of W .

The elastic scattering differential cross section is affected sensitively by $V(r_{\max})$, where $r_{\max} = 11$ fm, and to some extent, by a_R , although, since the real diffuseness and surface absorption both affect the large-angle scattering in similar ways, an ambiguity exists between these latter two quantities. The energy dependence of this correlation between a_R and $W(r_{\max})$ is seen most clearly in Fig. 15. As the energy is reduced, the flux attenuation by the barrier decreases faster than that corresponding to surface absorption, which is characterized by $W(r_{\max})$. Thus the different potentials, which are "equivalent" at 22 MeV (see Table IV), differ quite considerably in their predictions at lower energies, the increase in cross section due to high surface absorption overcompensating the decrease in barrier penetration due to an increase in a_R .

Normally, none of the α particles which have penetrated the barrier reappear, because of the absorption inside the nucleus and the difficulty of repenetrating the barrier. If, by reducing W_0 to a few MeV, the interior absorption is made extremely weak, sizeable oscillations are predicted at forward scattering angles. These are seen only weakly ($\pm 0.5\%$) in the 22-MeV ^{209}Bi data between 30 and 60° (see Fig. 2), and it may be safely assumed that the α particles which do penetrate the barrier are effectively removed from the entrance channel.

The most accurately determined quantity is the real potential form factor near the peak of the potential barrier, which is the sum of the nuclear and Coulomb parts for $l=0$ waves. The Coulomb potential is customarily taken to be that due to a point charge or a uniformly charged sphere, whereas the actual Coulomb potential is due to the interaction between two finite and diffuse charge distributions. A calculation using measured charge densities has shown that for separations greater than 8 fm the actual Coulomb potential differs insignificantly from that due to two point charges. Thus, the experimental result may be expressed equally well by quoting values of either the radius r_B and height V_B of the barrier peak, or the magnitude $V(r_B)$ and fall-off parameter $b(r_B) = -V dr/dV_{r=r_B}$ of the real nuclear potential. The uncertainty in V_B is related directly to that in $V(r_B)$, and the uncertainty in r_B depends on uncertainties in $b(r_B)$, and to a lesser extent,

in $V(r_B)$. Using values determined in this experiment for $V(r_{\max})$ and $b(r_{\max})$, one obtains $V_B = 20.63 \pm 0.08$ MeV and $r_B = 11.01 \pm 0.06$ fm for ^{209}Bi .

This sensitivity of low-energy α scattering to the real potential barrier has been pointed out also by Goldring *et al.*²² These authors quote even smaller uncertainties in V_B and r_B of ± 0.04 MeV and ± 0.04 fm, respectively. This may be because their measurements were analyzed using a four-parameter optical model, with searches involving one or, at most, two free parameters. Indeed, in the present studies, it was found that the number of acceptable parameter sets is greatly reduced if fewer parameters are allowed to vary. For example, the coupling between the real and imaginary potentials was seen only after their geometries were uncoupled and searches made with up to six free parameters. On the other hand, one may be able to assume that the geometries and relative potential strengths are similar from isotope to isotope, so that differences between neighboring nuclei can be established with restricted searches even if there is less certainty about the absolute determination of the nuclear tail.

IV. MICROSCOPIC MODEL ANALYSIS

A. Folding-model representation

The past few years have seen renewed interest in α scattering following the encouraging results of several groups using rather simple microscopic representations of the α -nucleus interaction. These studies use an approach similar to that developed by Greenlees, Pyle, and Tang²³ for the nucleon-nucleus interaction. The real potential is calculated by folding an effective two-body force V_{eff} representing the interaction between a nucleon and an α particle into the nuclear density distribution $\rho_m(r)$ of the target nucleus according to Eq. (3).

$$V(\vec{r}) = \int V_{\text{eff}}(\vec{r}' - \vec{r}) \rho_m(\vec{r}') d\vec{r}'. \quad (3)$$

The imaginary potential either is taken to have the same form as $V(r)$ or, more commonly, is independently parametrized.

Density distributions either are calculated using the shell model or are taken from the literature on electron scattering²⁴ and μ -mesic atom studies²⁵ which give quite accurate information about charge distributions, from which proton distributions may be determined. The neutrons are assumed either to have the same distribution as the protons, or estimates of the n - p difference are taken from, for example, analyses of nucleon scattering²⁶ or Coulomb energies.²⁷ Reasonably accurate infor-

mation is available for the gross features of the matter distribution, such as the mean square radius. The α -particle interaction on the other hand, is sensitive to the tail of the nuclear density well beyond the half-way radius, where not even the charge density is well determined.

Different forms have been taken for the two-body potential $V_{\text{eff}}(r)$. Often^{28,29} it is derived, in the spirit of the folding model by folding a nucleon-nucleon potential into the spatial distribution of the α particle. Occasionally³⁰ it is treated as a phenomenological form factor whose strength and range parameters are adjusted to fit the α -scattering data. These effective potentials do not give good fits to nucleon- α data, although the resulting folded potentials give quite good fits to α -nucleus scattering at forward angles.

A somewhat different point of view, outlined in the introduction, argues that in the low-density surface region the free nucleon- α interaction is the appropriate one to use for V_{eff} . This approach has been applied in a recent analysis of α scattering,³¹ and gives fits to accurate data over the full angular range whose quality surpasses those of a six-parameter conventional optical-model analysis.

If this approach is valid, it should be particularly appropriate in the present case since the low energy and high Coulomb barrier restrict the projectile to an even lower matter density region than is the case at higher energies on a medium-weight target nucleus.

The 22-MeV ^{209}Bi data were fitted using the following form for V_{eff} :

$$V_{\text{eff}} = 42.5[1 + \exp(r - R)/0.34]^{-1} \text{ MeV}, \quad (4)$$

where $R = (1.43 - 0.009E)A^{1/3}$ fm and E is the lab nucleon energy. Equation (4) is the central part of a nucleon - α potential which was derived by fitting simultaneously an extensive set of experimental data for incident nucleon energies below 11 MeV.^{19,31} The matter density was taken to be similar to that of Nolen and Schiffer,²⁷ which is consistent with experimental determinations of Coulomb energies and electron scattering. The difference between the neutron and proton root-mean-square radii, $\Delta n\rho$, for this distribution is 0.115 fm, which is quite small.

In the calculations, the effective nucleon energy E was taken to be zero, which corresponds classically to the α -particle energy near r_{\max} . In the extreme tail of the nucleus, the effect of the nucleon Fermi momentum is expected to be rather small, and, since the energy dependence of V_{eff} is quite weak, the procedure will have a negligible effect on the shape of the form factor and at most may introduce a systematic error of a few per-

cent in the magnitude of $V(r)$. This energy dependence could be readily included should any theoretical argument warrant it.

The result is a potential which matches the phenomenological one extremely closely at 11 fm both in magnitude and fall off. The accurate 22-MeV scattering and reaction cross-section data were fitted using this form factor, allowing only the central strength V_0 and the three imaginary parameters to vary. The best fit was achieved with $\chi^2/\rho t \approx 1.4$ which is comparable with that of the best six-parameter regular fits. In addition, the final value of V_0 was only 2% greater than the initial calculated value, and this is well within the inherent uncertainties of the model. It may be partly fortuitous that these parameters used for V_{eff} and ρ_m work so well, but it does demonstrate the consistency of the model, not only for medium weight nuclei,³¹ but for heavy nuclei as well.

B. Target-matter densities

Given the validity of the simple folding model, it follows that, if V_{eff} is known, or assumed, and if $V(r)$ is determined experimentally, then, in principle, one can determine $\rho_m(r)$, the nuclear

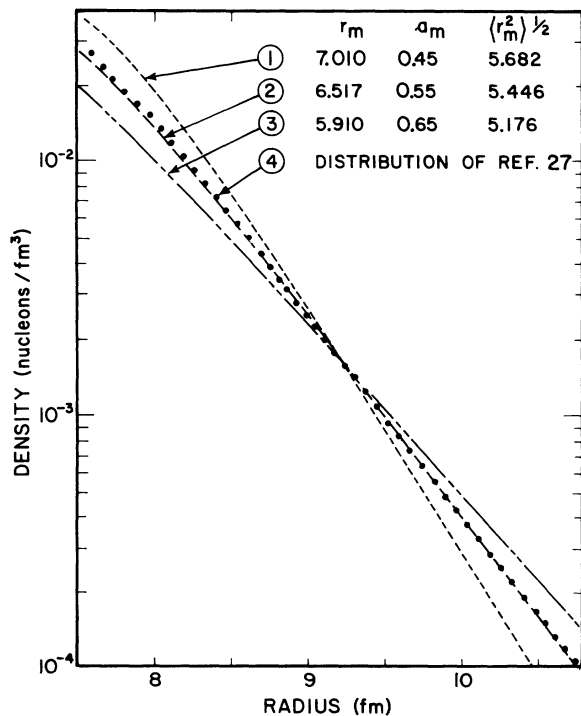


FIG. 17. Surface matter distributions for ^{209}Bi obtained using the folding model as described in the text. The dotted curve is the distribution for ^{208}Pb given by Nolen and Schiffer (Ref. 27), which is expected to be quite similar. Note that the nucleon size is included in these distributions.

density distribution of the target nucleus, via Eq. (3). This procedure is unlikely to be fruitful in the nuclear interior where the simple model almost certainly is invalid. A recent criticism³² of the folding method as it is usually applied suggests that a density-dependent two-body interaction is essential in relating nucleon-nucleus potentials with experimental densities. Such refinements are not expected to affect the interpretation at the low energies of the present study, and the simple form we use should give useful information in the surface region where the model is more applicable and moreover where the potential is best known.

Figure 17 shows those surface-density form factors which generate a range of acceptable equivalent α -nucleus potentials, each of which has a strength of 1.1 MeV at r_{max} using the V_{eff} of Eq. (4) with $E=0$ MeV. Due to the finite range of V_{eff} , $V(r)$ at 11 fm determines $\rho_m(r)$ near $r=9.2$ fm, which equals 1.7×10^{-3} nucleon/fm³. If $E=3$ MeV, the value becomes 1.85×10^{-3} nucleon/fm³. These are, in either case, low densities, less than 1% of the central value and which correspond to an average nucleon separation of about 9 fm.

There has been considerable discussion recently^{33,26} about Δnp , the difference in the rms radii of neutrons and protons in lead. The latest acceptable values lie between 0.0 and 0.2 fm. Assuming the validity, of the folding procedure, the present studies determine the nuclear-matter density in a localized region near 9 fm, and this in itself does not furnish a good measurement of Δnp .

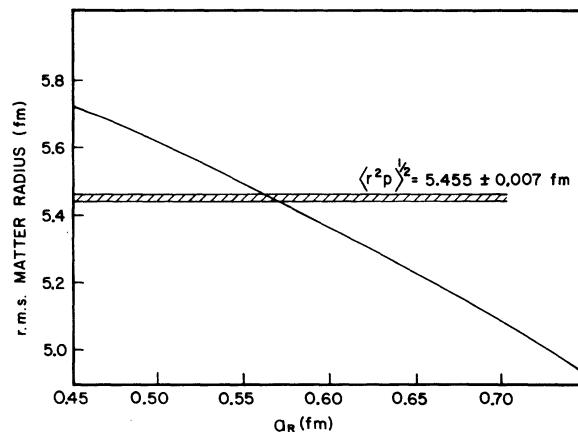


FIG. 18. The dependence of the root-mean-square radius of the ^{209}Bi matter distribution on the real diffuseness a_R of the real potential it generates via Eq. (3), given that the real potential at 11 fm equals 1.1 MeV. A Woods-Saxon form for the matter distribution is assumed. The cross-hatched region marks the proton rms radius for ^{209}Bi given by Acker *et al.* (Ref. 25).

However, if one takes V_{eff} as given by Eq. (4), and assumes a particular shape for $\rho_m(r)$ (a Woods-Saxon form factor may be appropriate for ^{208}Pb or ^{209}Bi), then fitting both the magnitude and fall-off rate of the surface potential completely determines $\rho_m(r)$ and hence $\langle r_m^2 \rangle$. Figure 18 shows the dependence of $\langle r_m^2 \rangle^{1/2}$ as a function of a_R , the effective diffuseness of the calculated α -nucleus potential. In each case, $V(r_{\text{max}}) = 1.1$ MeV. The best fits to the data were obtained with $a_R = 0.55$ fm which corresponds to a rms matter radius which is essentially the same as that of the proton distribution, and implies that Δn_p is close to zero. Curve 2 in Fig. 17 represents such a density distribution.

The fall off of this density distribution near 9 fm is very similar to that of the calculated distribution of Nolen and Schiffer²⁷ (dotted curve in Fig. 17), for which the behavior at large radii is determined largely by the binding energies of the last few nucleons, and not by the details of the potential well. An experimental value of $\Delta n_p = 0$ for curve 2 of Fig. 17 is not inconsistent with $\Delta n_p = 0.115$ fm for the distribution of Ref. 27, because the forms of the two distributions are not exactly the same. This underlines the danger in attempting to determine rms radii from analyses of low-energy α -particle scattering alone.

These general conclusions are modified only slightly if other shapes are used for V_{eff} . Batty, Friedman, and Jackson³⁴ have reviewed recently the different Gaussian forms: $V = V_0 e^{-k^2 r^2}$, which have been used to represent the α -nucleon potential. They find that, of those potentials which give moderately good fits to the α -nucleon data, the one for which $V_0 = 53.8$ MeV and $k = 0.526$ fm⁻¹ gives good fits to results on ^{208}Pb and ^{58}Ni when folded into density distributions calculated using the simple shell model. In the present case, this two-body potential gives target-density form factors which intersect 8.8 fm, where the density equals 3.3×10^{-3} nucleon/fm³, which is still quite low. At 9.2 fm the densities are essentially the same as those given by the potential of Eq. (4).

Other forms for V_{eff} , considered in Ref. 34 give densities which differ significantly from those of Fig. 17. These potentials do not fit the α -nucleon data at all, and therefore it is difficult to justify their use without questioning the validity of the simple folding procedure.

However, even if the details of V_{eff} are unknown, the model does give a straightforward method for

determining differences in the tails of density distributions for neighboring nuclei.

V. CONCLUSIONS

The α interaction with the heavy nuclei ^{208}Pb and ^{209}Bi at energies close to the Coulomb barrier is not significantly different from that at higher energies. It is well described in terms of a folding model which uses an effective two-body force obtained by fitting α -nucleon data, and which has been shown to give an improved fit to scattering by medium-weight nuclei over that of a regular six-parameter optical model.

Although quite a good over-all fit can be obtained to all the data, potentials which give optimum fits at 22 MeV predict too much reaction cross section at lower energies. This may indicate either a sharp decrease in the surface absorption or the competition of radiative capture with neutron emission close to the neutron threshold.

In terms of the folding model, the fact that the data only specify the potential near the barrier peak at 11 fm leads to a knowledge of the matter density near 9.2 fm of 1.7×10^{-3} nucleons/fm³. The slope is not well determined in this experiment, although the minimum in χ^2 occurs near $a_R = 0.55$ fm which is close to the other values quoted in α -Pb analyses. Assuming the matter distribution has a Woods-Saxon form this gives an rms matter radius $\langle r_m^2 \rangle^{1/2} = 5.48$ fm, which is entirely consistent with other determinations of this quantity.

Although work near the barrier is dominated by Coulomb scattering, there are some advantages in working at such low energies. Cross sections can be measured accurately, and the low value of W in the tail reduces the sensitivity to the imaginary parameters and testifies to the expected low breakup probability of the α particle. Although polarization and exchange may be more important at low velocities, that there is no evidence for these effects in the energy dependence of the α interaction may be due to the typically very low nucleon density with which the α particle interacts.

Thus, the fact that the α particle is less sensitive to the nuclear core at these low energies, justifies the assumptions of the simple folding model, and implies that an analysis may yield information rather specific to a region of nuclear matter which is difficult to study in other ways.

- *Work supported in part by the Atomic Energy Commission Contract No. AT(11-1)-2165.
- †Present address: University of Manchester, Manchester M13 9PL, United Kingdom.
- ¹G. Igo, Phys. Rev. 115, 1665 (1959).
- ²A. R. Barnett and W. R. Phillips, Phys. Rev. 186, 1205 (1969).
- ³R. A. Broglia, J. S. Lilley, R. Perazzo, and W. R. Phillips, Phys. Rev. C 1, 1508 (1970).
- ⁴W. J. Ramler, J. Wing, D. J. Henderson, and J. R. Huizenga, Phys. Rev. 114, 154 (1959).
- ⁵E. L. Kelly and E. Segre, Phys. Rev. 75, 999 (1949).
- ⁶A. R. Barnett, J. H. Broadhurst, and R. W. Goodwin, Annual Report, J. H. Williams Laboratory of Nuclear Physics, University of Minnesota, 1969 (unpublished).
- ⁷P. A. Tove, Ark. Fys. 13, 549 (1958).
- ⁸I. Perlman, F. Asaro, A. Ghiorso, A. Larsh, and R. Latimer, Phys. Rev. 127, 917 (1962).
- ⁹P. L. Reeder, Phys. Rev. C 1, 721 (1970).
- ¹⁰F. N. Spiess, Phys. Rev. 94, 1292 (1954).
- ¹¹J. R. Huizenga, R. Chaudhry, and R. Vandebosch, Phys. Rev. 126, 210 (1962); I. Halpern and W. J. Nicholson, Progress Report, University of Washington, Seattle, 1968 (unpublished), p. 10.
- ¹²E. T. Chulick and J. B. Natowitz, Nucl. Phys. A173, 487 (1971).
- ¹³F. D. Becchetti, Jr., M. S. thesis, University of Minnesota, 1968 (unpublished); F. D. Becchetti and G. W. Greenlees, Phys. Rev. 182, 1190 (1969).
- ¹⁴D. C. Weisser, J. S. Lilley, R. K. Hobbie, and G. W. Greenlees, Phys. Rev. C 2, 544 (1970).
- ¹⁵J. S. Blair, Phys. Rev. 108, 827 (1957).
- ¹⁶This latter conclusion was modified somewhat when the accurate ²⁰⁹Bi scattering data at 22 MeV were included. The results are fitted best with a slightly smaller value of a_R than the minimum shown in Fig. 11.
- ¹⁷J. O. Rasmussen, in *Alpha, Beta and Gamma-Ray Spectroscopy*, edited by K. Siegbahn (North-Holland, Amsterdam, 1965), Vol. I.
- ¹⁸G. R. Satchler, L. W. Owen, A. J. Elwyn, G. L. Morgan, and R. L. Walter, Nucl. Phys. A112, 1 (1968).
- ¹⁹P. Mailandt, Ph.D. thesis, University of Minnesota, 1971 (unpublished).
- ²⁰G. J. Pyle, J. H. Williams Laboratory of Nuclear Physics, University of Minnesota Report No. COO-1265-64, 1968 (unpublished); see also G. W. Greenlees, G. J. Pyle, and Y. C. Tang, Phys. Rev. 171, 1115 (1968).
- ²¹R. M. Drisko, G. R. Satchler, and R. H. Bassel, Phys. Lett. 5, 347 (1963).
- ²²G. Goldring, M. Samuel, B. A. Watson, M. C. Bertin, and S. L. Tabor, Phys. Lett. 32B, 465 (1970).
- ²³G. W. Greenlees, G. J. Pyle, and Y. C. Tang, see Ref. 20.
- ²⁴J. L. Friar and J. W. Negele, Nucl. Phys. A212, 93 (1973).
- ²⁵H. L. Acker, G. Backenstoss, C. Daum, J. C. Sens, and S. A. DeWit, Nucl. Phys. 87, 1 (1966); C. S. Wu and L. Wilets, Annu. Rev. Nucl. Sci. 19, 527 (1969); S. Devons and I. Duerdoth, in *Advances in Nuclear Physics*, edited by M. Baranger and E. Vogt (Plenum, New York, 1969), Vol. 2, p. 295.
- ²⁶G. W. Greenlees, M. Makofske, and G. J. Pyle, Phys. Rev. C 1, 1145 (1970).
- ²⁷J. A. Nolen and J. P. Schiffer, Annu. Rev. Nucl. Sci. 19, 471 (1969).
- ²⁸C. J. Batty and E. Friedman, Phys. Lett. 34B, 7 (1971).
- ²⁹D. F. Jackson, Phys. Lett. 14, 118 (1964); A. M. Bernstein, in *Advances in Nuclear Physics*, edited by M. Baranger and E. Vogt (Plenum, New York, 1970), Vol. 3, p. 325; A. Budzanoski, A. Dudek, K. Grotowski, and A. Strzalkowski, Phys. Lett. 32B, 431 (1970).
- ³⁰D. F. Jackson and V. K. Kumbhavi, Phys. Rev. 178, 1626 (1969).
- ³¹P. Mailandt, J. S. Lilley, and G. W. Greenlees, Phys. Rev. Lett. 28, 1075 (1972); Phys. Rev. C 8, 2189 (1973).
- ³²W. D. Myers, Nucl. Phys. A204, 465 (1973).
- ³³B. W. Allardyce *et al.*, Nucl. Phys. A209, 1 (1973); A. M. Bernstein and W. A. Seidler, Phys. Lett. 39B, 583 (1973); B. Tatischeff and I. Brissaud, Nucl. Phys. A155, 89 (1970); B. Tatischeff, I. Brissaud, and L. Bimbot, Phys. Rev. C 5, 234 (1972).
- ³⁴C. J. Batty, E. Friedman, and D. F. Jackson, Nucl. Phys. A175, 1 (1971).